Enabling 6C Fast Charging of Li-ion Batteries with Graphite/Hard Carbon Hybrid Anodes

*Kuan-Hung Chen[1], Vishwas Goel[1], Min Ji Namkoong[2], Markus Wied[3], Simon Müller[3], Vanessa Wood[3], Jeff Sakamoto[1,2], Katsuyo Thornton[1], Neil P. Dasgupta[1,2,]**

[1] Department of Materials Science and Engineering, University of Michigan, Ann Arbor, MI, 48109, USA
[2] Department of Mechanical Engineering, University of Michigan, Ann Arbor, MI, 48109, USA
[3] Department of Information Technology and Electrical Engineering, ETH, Zurich 8092, Switzerland

E-mail: ndasgupt@umich.edu

Keywords: Batteries, Fast-charging, Graphite, Lithium Plating, Modeling

Abstract:

Li-ion batteries that can simultaneously achieve high energy density and fast charging are essential for electric vehicles. Graphite anodes enable a high energy density, but suffer from an inhomogeneous reaction current and irreversible Li plating during fast charging. In contrast, hard carbon exhibits superior rate performance but lower energy density owing to its lower initial Coulombic efficiency and higher average voltage. In this work, we overcome these tradeoffs by fabricating hybrid anodes with uniform mixtures of graphite and hard carbon, using industrially-relevant multi-layer pouch cells (> 1 Ah) and electrode loadings (3 mAh/cm^2). By controlling the graphite/hard carbon ratio, we show that battery performance can be systematically tuned to achieve both high energy density and efficient fast charging. Pouch cells with optimized hybrid anodes retain 87% and 82% of their initial specific energy 500 cycles of 4C and 6C fast-charge cycling, respectively. This is significantly higher than the 61% and 48% specific energy retention with graphite anodes under the same conditions. The enhanced performance is attributed to improved homogeneity of the reaction current throughout the hybrid anode, which is supported by continuum-scale modeling. This process

is directly compatible with existing roll-to-roll battery manufacturing, representing a scalable pathway to fast-charging.

1. Introduction

Lithium-ion (Li-ion) batteries with both high energy density and fast-charge capability are needed to accelerate the widespread use of electric vehicles (EVs). However, current high-energy-density EV batteries are unable to achieve fast charging without adversely impacting battery performance and safety. When Li-ion batteries are charged at high rates, increased cell polarization results in limited energy utilization, increased capacity fade, excessive heat generation, and other deleterious effects.[1–3] These consequences limit the charging time of the state-of-the-art EV batteries. Therefore, there is an unmet need to develop Li-ion technology that can simultaneously achieve high energy density and efficient fast charging. To address these technological challenges, the U.S. Department of Energy (DOE) has identified performance targets for extreme fast charging of batteries with > 180 Wh/kg specific energy within a 10-min charging time and < 20% energy fade over 500 cycles.

Graphite has been predominantly used as the anode material in state-of-the-art Li-ion batteries due to its stable electrochemical performance and high specific capacity.[4] During charge/discharge processes, graphite displays well-defined voltage plateaus at low potentials (< 0.2 V vs. Li/Li^+) as well as relatively-high first-cycle (initial) and subsequent cycling Coulombic efficiencies. These properties make graphite an attractive material for achieving high-energy-density Li-ion batteries. As a result, graphite anodes have been commercialized since the beginning of Li-ion industry and continue to play a critical role in EV battery technology.[5–7]

While the low redox potential of graphite promotes higher cell energy density, it also raises concerns when graphite anodes are subjected to fast-charge conditions. During fast charging, high current densities induce large anode polarizations as a consequence of transport and kinetic limitations.[8–10] These limitations can spatially vary throughout the anode thickness/volume, leading to a spatially inhomogeneous charging current.[9–13] As a result, poor electrode utilization and a non-uniform state-of-charge occur during fast charging, with large portions of the anode near the current collector not being utilized (**Scheme 1**).[9,13] Moreover, the graphite anode can reach electrochemical potential values more negative than the thermodynamic potential of Li metal (< 0 V vs. Li/Li^+), making Li plating a favorable process. The formation of metallic Li on graphite anode surface has been shown to cause irreversible loss of Li inventory, leading to significant cell capacity fade.[3,14,15]

The high anode polarizations during fast charging have been attributed to several physicochemical processes, including (1) ionic transport in the electrolyte phase, (2) reaction kinetics at the graphite/electrolyte interface, and (3) solid-state Li diffusion in graphite particles.[3,9,16,17] Consequently, previous research efforts have focused on enhancing ionic transport in porous electrodes by reducing electrode tortuosity[13,18,19], improving interfacial and transport kinetics through new electrolyte and/or additive design[20–22], increasing the cell temperature during charging[16], and applying coatings to the anode surface[23].

While improved electrochemical performances have been demonstrated in these approaches, achieving long-term cycling (≥ 500 cycles) of graphite-based Li-ion batteries with high capacity loading (≥ 3 mAh/cm^2) under ≥ 4C fast-charge conditions at room temperature still remains challenging. In addition, developing scalable processing approaches that are directly compatible with existing Li-ion manufacturing with minimal additional cost and implementation time is also important to accelerate commercialization.

In contrast to graphite, which has long-range order in its crystallographic structure, hard carbon is defined as non-graphitizable carbon consisting of highly disordered carbon layers (Scheme 1). During the lithiation process, Li can be inserted in between the disordered carbon sheet domains as well as in the micro-pores of the hard carbon structure.[24–26] When used as the anode material for batteries, hard carbon has the following characteristics: (1) low material density (1.6 g/cm^3) compared to graphite (2.2 g/cm^3), (2) sloping charge/discharge voltage profile between 0-1.2 V vs. Li/Li$^+$, (3) low initial Coulombic efficiency (< 80%), and (4) enhanced power performance.[4,7,25–27] The low initial Coulombic efficiency of hard carbon has been attributed to solid electrolyte interphase (SEI) formation[4,27,28], trapped Li in micro-pore structures[29], and reactions between Li and surface functional groups.[30] This large first-cycle irreversible capacity loss translates into a significant energy density penalty. Therefore, while the improved rate performance of hard carbon is attractive for high-power applications[31], poor initial Coulombic efficiency, along with a high redox potential and low density, have limited its adoption in high-energy-density battery systems.[4,32] Therefore, a tradeoff between the energy density and power performance is present (Scheme 1).

In this study, we introduce a strategy to overcome this energy/power density tradeoff by fabricating uniform mixtures of graphite/hard carbon active material particles into a bulk hybrid anode. By doing so, it is possible to balance the desirable characteristics of both materials and rationally tune the electrode properties in a synergistic manner to improve current homogeneity and reduce Li plating during fast charging, while maintaining sufficiently-high cell energy densities (Scheme 1).

Previous studies on the concept of graphite/hard carbon hybrid anodes have been largely limited to surface modifications of the active materials prior to electrode fabrication, such as

coating hard carbon onto graphite particle surfaces to improve rate capability[33,34] or applying graphite micro-crystallites onto hard carbon particles to improve initial Coulombic efficiency and reversible capacity.[35] While mixing of varying carbonaceous materials have been studied for battery systems[36–38], the charge rates in these studies have not addressed the DOE and industry fast-charge targets (10-min charging time).

In this work, we demonstrate hybrid anodes fabricated by mixing graphite and hard carbon to achieve fast-charging Li-ion batteries with energy density > 180 Wh/kg, using industrially relevant multi-layer pouch cells (> 1 Ah) and electrode capacity loadings (3 mAh/cm^2). Standard roll-to-roll slurry casting was performed to fabricate the hybrid anodes, demonstrating compatibility with existing Li-ion manufacturing. By tuning the blend ratio of graphite and hard carbon, it is shown that the battery performance can be systematically tuned to simultaneously achieve high energy density and fast charging. As a result of the optimized hybrid anode design, we demonstrate pouch cells with 87% and 82% specific energy retention after 500 cycles of 4C and 6C fast-charge cycling using hybrid anodes, compared to 61% and 48% for cells using graphite anodes under the same conditions. In addition, while the optimized hybrid cells show 10% lower initial specific energy compared to the graphite cells, the remaining specific energy after 500 cycles of fast charging is 27% larger at 4C and 53% larger at 6C.

Systematic electrochemical analysis was performed to demonstrate the efficacy of the hybrid anode design, and synchrotron tomography was employed to analyze the electrode microstructures. Continuum-scale electrochemical simulations were further performed to provide insights into the enhanced fast-charge performance, which is attributed to the improved homogeneity in reaction current distribution throughout the hybrid anode. The cell

performance presented in this work addresses the DOE goal for fast-charging high-energy-density Li-ion batteries.

2. Results and Discussion

2.1. Fabrication of Hybrid Anodes

Graphite/hard carbon hybrid anodes were prepared using a pilot-scale roll-to-roll processing facility at the University of Michigan Battery Lab (further details in Supporting Information). Five graphite/hard carbon blend ratios were investigated in this work, namely, graphite/hard carbon = 100/0, 75/25, 50/50, 25/75, and 0/100 (weight ratios). The resulting hybrid anodes are described below as graphite, Gr-75, Gr-50, Gr-25, and hard carbon, respectively. A capacity loading of 3 mAh/cm^2 was controlled for all 5 types of anodes with a calendered porosity of 31-33%.

Scanning electron microscopy (SEM) was performed to examine the morphology of the prepared hybrid anodes. **Figure 1a** shows a top-down image of the graphite anode. The graphite particles have an ellipsoidal shape with an average particle size of 7.8 μm (Figure S1). Figure 1e shows an image of the hard carbon anode. Compared to the graphite, hard carbon particles have a more isotropic shape. The hard carbon also displays a smaller average particle size of 3.3 μm (Figure S1). For Gr-75 (Figure 1b), Gr-50 (Figure 1c), and Gr-25 (Figure 1d) hybrid anodes, the SEM images show that both graphite and hard carbon particles were homogeneously distributed throughout the anode thickness (cross-sectional SEM images shown in Figure S2).

To further confirm the homogeneous mixing of graphite and hard carbon, optical microscopy was performed. The anodes were lithiated at a C/50 rate, and then disassembled and imaged.

At 100% state-of-charge, the color of graphite changes from grey to gold[39,40], whereas the color of hard carbon remains dark grey. Therefore, by inspecting the distribution of the gold graphite particles in the hybrid anodes, the homogeneous blend of graphite/hard carbon can be visualized (Figure 1f-o).

2.2. Synchrotron Tomography

Synchrotron tomography was performed on the graphite, Gr-50, and hard carbon electrodes to analyze three-dimensional (3-D) microstructures, following methods described in the previous studies.[41,42] **Figure 2a-c** show 3-D representations of the three electrodes obtained by segmenting the tomography data (details in Supporting Information). The tomography data show variations in the porosity from 30% to 35%. In addition to the grey-scale value information provided by the tomographic imaging, the segmentation threshold was adjusted to yield a porosity of 31-33% to match the measured capacity loading and thickness values (Figure 2d-f). While the average porosity values are ~32% for all three electrodes after the adjustment, differences in the variation of local porosity can be identified.

Porosity maps (Figure S3) show the local variations found across the entire electrode microstructures. A scale-space analysis on the porosity was performed to ensure the chosen sub-volume size is representative for all three electrodes (Figure S4). Overall, the Gr-50 electrode has the most uniform porosity distribution shown by its narrow histogram (Figure 2e), followed by that of hard carbon (Figure 2f).[43] In contrast, the porosity histogram of the graphite electrode is significantly wider, ranging from 30%-35% (Figure 2d). These localized variations in electrode microstructures may impact the local current density within the electrodes.[44]

In addition, microstructural features such as particle and pore size can be identified, as shown in Figure 2a-c. The graphite electrode shows the largest pores with elongated shapes, whereas the hard carbon electrode has the smallest pores with a more circular shape. These observations are quantified by comparing the average pore diameters (Figure S4). The average pore diameter reduces from 1.02 ± 0.03 μm for the graphite electrode to 0.72 ± 0.01 μm for the hard carbon electrode. The average pore diameter of the Gr-50 electrode (0.82 ± 0.01 μm) is closer to the value of the hard carbon electrode. It is noted that due to the limitation in resolution, which was calculated to be 317 nm (~2 voxels) by means of the Fourier shell correlation[45], pores smaller than 700 nm (3-4 voxels wide) cannot be reliably quantified.

Overall, the tomography analysis demonstrates that, while the graphite and hard carbon are uniformly blended throughout the bulk of the electrode, subtle differences in the local microstructures can be observed.

2.3. Voltage and Initial Coulombic Efficiency Analysis

To characterize the voltage profile of the hybrid anodes, three-electrode measurements were performed using a Li metal reference electrode (further details in Supporting Information). **Figure 3a** shows anode potential vs. state-of-charge (SOC) profiles of all 5 anodes during charging at a C/10 rate (further details in Figure S7). As shown in the figure, the graphite anode shows an initial drop in potential to 0.2V, followed by well-defined voltage plateaus. In contrast, the hard carbon anode displays a sloping voltage trace as the potential gradually decreases from 1.2 V to 0 V. For Gr-75, Gr-50, and Gr-25 hybrid anodes, the anode potentials are observed at intermediate values between the graphite and hard carbon voltage profiles.

Figure 3b shows a magnified view of the voltage profiles between 0-0.3 V vs. Li/Li$^+$. It can be clearly observed the graphite anode displays three characteristic plateaus at 0.2 V, 0.12 V, and 0.08 V, which can be attributed to transitions between staged phases during Li intercalation.[46,47] On the other hand, hard carbon does not exhibit any voltage plateau. The high-potential region of the sloping voltage profile has been associated with Li insertion into interlayer space between carbon layers, and the low-potential region has been attributed to Li storage in the micro-pores of hard carbon.[24]

For Gr-75, Gr-50, and Gr-25 hybrid anodes, the voltage traces display features from both graphite (voltage plateaus) and hard carbon (sloping potential), indicating that both materials are electrochemically active in the hybrid anodes during charging. With higher graphite content in the hybrid anodes, increasing width in voltage plateaus is observed, which is consistent with a larger fraction of the capacity provided by graphite. It is also noted that while the voltage plateaus associated with graphite occur at approximately the same average potential values regardless of the varying graphite/hard carbon blend ratios (Figure 3b), the slope of the plateaus increases with increasing hard carbon content. Furthermore, the onset of the plateaus is observed to be shifted to higher SOCs with increasing hard carbon content. This is consistent with the more positive potential of hard carbon at low SOC, which will cause hard carbon to preferentially lithiate during the early stages of charging the hybrid anodes. These effects, and their impact on fast charging, will be discussed further in the modeling section below.

To quantify the initial irreversible capacity of the hybrid anodes, initial Coulombic efficiency (ICE) during the first charge/discharge cycle was measured using a 3-electrode cell. Figure 3c shows the ICE vs. graphite content. The graphite anode displayed a high ICE of 88%, whereas the hard carbon anode ICE was only 76%. For Gr-75, Gr-50, and Gr-25 hybrid anodes, the

corresponding ICE follows a linear relationship as a function of the graphite content (Figure 3c), indicating that the ICE can be tuned by adjusting the blend ratios of graphite and hard carbon.

The ICE was further measured in full cells, where multi-layer pouch cells (> 1 Ah) were fabricated. The hybrid anodes were assembled with NMC-532 cathodes (N/P ratio of 1.16 ± 0.1) to make 5 different types of pouch cells, namely, graphite, Gr-75, Gr-50, Gr-25, and hard carbon cells. Pouch cells were cycled at a C/10 rate to measure the charge/discharge capacity during the first cycle (Figure 3d). As shown in the figure, while the first-cycle charge capacity of all 5 pouch cells is ~ 1.53 Ah, differences in the subsequent discharge capacity are observed (voltage traces shown in Figure S8). The ICE of the pouch cells is calculated and plotted in Figure 3c to compare with 3-electrode cell results. As shown in the figure, the pouch cell ICEs agree well with the 3-electrode measurements, with the exception of the pure graphite cell.

The discrepancy between the 3-electrode and pouch cells using graphite anodes can be explained by the ICE of the cathode. Winter et al. have shown that the first-cycle irreversible capacity of NMC cathodes can be attributed to kinetic limitations and irreversible processes, resulting in an ICE of 83-86%.[48] Recently, Whittingham et al. also demonstrated the first-cycle capacity loss of NMC-811 is due to slow kinetics and surface changes in the materials during the charge process.[49] Therefore, it can be inferred that for anodes exhibiting higher ICE than NMC cathodes, the overall full cell capacity and ICE will be limited by the cathode. To verify this point, the ICE of the NMC-532 cathode was further measured (to be 85%) using the 3-electrode cell setup and plotted in Figure 3c (dashed line). For this reason, the Gr-75 hybrid anode has the same full-cell ICE value as the pure graphite anode (Figure 3c),

which demonstrates that hybrid anodes with relatively low hard carbon content will not suffer significantly from an ICE penalty.

To demonstrate stable cycling of the hybrid anode under standard conditions, all 5 types of pouch cells were charged/discharged at a 1C/1C rate between 2.7-4.2 V (Figure S9). All pouch cells exhibit similar aging rates with high capacity retention of 95-96% after 200 cycles. This result indicates that there is minimal difference in performance between the cells using different hybrid anodes during standard-rate cycling after the initial cell formation cycles.

2.4. Fast-charge Cycling Performance

To evaluate the fast-charge capability of the hybrid anodes, a CC-CV charging protocol with a charging time cutoff was used (15 min for 4C and 10 min for 6C), following the DOE battery-testing guidelines (further details in Figure S10).[13,50] Pouch cells were cycled in a temperature-controlled chamber at 30°C.

Figure 4a shows the normalized cell capacity vs. cycle number plot during 4C (15-min) fast-charge cycling. The capacity shown here is the 1C discharge capacity after each 4C charge (following the DOE battery-testing guidelines), in order to reflect Li inventory loss and the remaining cyclable capacity. The y-axis is normalized to the first 4C charge cycle to facilitate a comparison of capacity retention among all 5 types of pouch cells. The graphite cell exhibits significant capacity fade during the first 50 fast-charge cycles. This initial non-linear decrease in capacity has been attributed to significant Li plating during fast charging[9,10,13,16,17], which corresponds to a dip in Coulombic efficiency during initial cycles (Figure S11). As cycling progresses, the capacity retention of the graphite cell levels off at 67% after 100 cycles, as the

significant Li inventory loss reduces the driving force for further Li plating.[3,13] The Gr-75 cell displays a similar trend with less capacity fade during fast-charge cycling, suggesting an improved rate performance in comparison to the graphite (Figure 4a). The capacity retention of the Gr-75 cell is 85% after 100 cycles of 4C fast charging.

In contrast, Gr-50, Gr-25, and hard carbon cells all exhibit stable 4C charging throughout the course of the test. The steep initial capacity drop observed in the graphite and Gr-75 cells is completely absent in these cells. As a result, the capacity retention of the Gr-50, Gr-25, and hard carbon cells after 100 cycles is approximately 96% (Figure 4a).

To further demonstrate the efficacy of the hybrid anode design, another batch of pouch cells were cycled at a 6C charge rate. As shown in Figure 4b, larger drops in capacity are observed for both the pure graphite and Gr-75 cells that 4C fast-charge cycling, with only 58% and 74% capacity retention after 100 cycles. The reduced capacity retention during 6C fast-charge cycling also corresponds to lower minimum Coulombic efficiency values when compared with 4C fast-charge cycling (Figure S11). This has been attributed to an increased amount of Li plating with increasing charge rates.[13] In contrast, the Gr-50, Gr-25, and hard carbon cells again exhibit stable cycling during 6C fast charging. The capacity retention is ~93% after 100 cycles (Figure 4b). It is also noted that compared to ionic resistance, the electronic resistance of the cells is much smaller and is not the limiting factor during cycling (Figure S16 in Supporting Information).

Figure 4c summarizes the capacity retention of all 5 types of pouch cells after 100 cycles of 4C and 6C fast charging. As shown in the figure, for hybrid anodes with increasing (> 50 wt.%) graphite content, lower capacity retention is observed. For hybrid anodes with < 50

wt.% graphite content, the cells exhibit stable performance with minimal capacity fade during 4C and 6C fast charging (Figure 4c).

While the normalized cell capacity plots (Figure 4a-c) facilitate direct comparisons of capacity fade (%), the first-cycle irreversibility needs to be accounted for, in order to demonstrate the total cell capacity. Therefore, Figure 4d and 4e further plot the measured discharge capacity (Ah) vs. cycle number during 4C and 6C cycling. While the graphite and Gr-75 cells display higher cell capacity after the formation cycles, they suffer from significant capacity fade upon fast charging. On the contrary, the Gr-50, Gr-25, and hard carbon cells exhibit stable cycling at both C-rates. Overall, the Gr-50 cells show the highest total cell capacity among all 5 types of cells after 100 cycles of 4C and 6C charging. Additionally, voltage trace plots at various stages of cycling are provided in Figure S12, which demonstrate that a stable voltage profile is observed for graphite content ≤ 50%.

Figure 4f summarizes the total cell capacity of the pouch cells after 100 fast-charge cycles. Considering both ICE during cell formation (Figure 3c-d) and capacity fade during fast charging (Figure 4a-c), it is demonstrated here that an optimal graphite/hard carbon blend ratio can be selected to maximize the accessible cell capacity during fast-charge cycling. For an anode loading of 3 mAh/cm^2 under 4C and 6C fast-charge conditions, our analysis indicates that the 50/50 graphite/hard carbon blend ratio provides the maximum performance within the set of ratios tested.

2.5. Post-mortem Morphology Analysis

To confirm that the capacity fade during fast-charge cycling is correlated with increased Li plating, post-mortem SEM analysis was performed on the pouch cells after 100 cycles of 4C

charging. Cells were fully discharged before disassembly. Photographs of the cycled anodes are shown in **Figure 5a-e**. A considerable amount of Li plating is observed on both the graphite and Gr-75 anodes, where Li deposits cover the entire anode surface (Figure 5a-b). The plated Li maintains a metallic silver luster, suggesting that during cycling the Li deposits can become isolated from the electrode surface, resulting in the formation of dead Li.[51] The SEI growth on the plated Li and irreversible dead Li formation thus cause a permanent Li inventory loss, leading to the observed capacity fade.[3,17,51] SEM images further show the extent of Li plating on the graphite and Gr-75 anodes, where the electrode surface is covered with dead Li, and no underlying active material particles can be observed from a top view (Figure 5f-g). Cross-sectional SEM images also show the Li plating (false-colored in yellow) on the anode surface (Figure 5k-l). An increase in the dead Li thickness is observed with increasing graphite content, which is consistent with the increased capacity fade during fast-charge cycling (Figure 4a).

In contrast, the cycled Gr-50, Gr-25, and hard carbon anodes maintain a pristine surface, with no evidence of Li plating (Figure 5c-e). Both top-down (Figure 5h-j) and cross-sectional (Figure 5m-o) SEM images show the electrode surface and active particles remain clean and intact after extended fast-charge cycling. The post-mortem morphology is thus in a good agreement with the electrochemical performance (Figure 4).

2.6. Continuum-scale Electrochemical Simulations

To provide mechanistic insights for the observed improvement in rate performance of the hybrid anodes, continuum-scale simulations based on porous electrode theory[52,53] were conducted. In particular, we focused on the spatial variation in local reaction current density throughout the anode thickness, and the consequences of this heterogeneity on the propensity

for Li plating. The model was parameterized by matching the simulated voltage vs. capacity curves with the corresponding three-electrode measurements for the three anodes at six different C rates. More details about the model, including equations, parameters, and validation are described in the Supporting Information.

Galvanostatic charging of the graphite, Gr-50, and hard carbon anodes at 4C and 6C charging were simulated, and the results for 4C are summarized in **Figure 6** (6C results are provided in Figure S21). The simulations were terminated when the anode voltage (vs. Li metal reference) reached 0 V, below which Li plating may occur. Thus, these simulations correspond to the initial portion of the CC charging step in the experiments. A comparison of the simulated voltage vs. time curves for the three anodes is shown in Figure 6f. The hard carbon anode maintains a voltage above 0 V for the longest time, followed by the Gr-50 and graphite anodes.

To explain the difference in the performance of the three anodes, we examined the evolution of the local reaction current density (Figure 6a-e), as defined by reaction current per unit volume within each anode. The reaction current density is obtained by multiplying the reaction flux at the surface of the active material particles, the surface area of the particles per unit volume of the electrode, and Faraday's constant (see the definition of R_v in Supporting Information).

For the graphite anode (Figure 6a), it can be observed that the current density distribution becomes highly inhomogeneous after ~20 seconds of charging, with most of the reaction taking place in the region near the anode/separator interface. The peaks observed in the reaction current density arise because of the plateaus observed in the graphite OCV.[13] As mentioned earlier, a highly inhomogeneous current distribution results in a large anode

overpotential, thereby resulting in an earlier termination of the simulation. Moreover, the high reaction current magnitude causes graphite particles near the anode/separator interface to lithiate much faster than the rest of the anode. When the surface of the graphite particles near the anode/separator interface becomes saturated with Li, it becomes susceptible to Li plating as the charging is continued.[54–56] Therefore, due to the inhomogeneous current density distribution, the graphite anode has a higher propensity for Li plating during fast charging.

In contrast, the distribution of the reaction current density is much more uniform in the hard carbon anode during 4C charging (Figure 6c). This results in a smaller overpotential in the anode, which allows it to maintain current at a potential higher than 0 V for a longer time. Moreover, the homogeneous distribution lowers the local reaction current and thus reduces saturation of the particle surface near the anode/separator interface. This is consistent with the improved rate performance and absence of Li plating observed experimentally. The more homogeneous current density distribution in the hard carbon anode arises from the complex interplay between thermodynamics, reaction kinetics, and electrochemistry.[57] In particular, the sloping OCV profile can homogenize the current density distribution[58,59], while any transport limitations tend to increase the inhomogeneity. Due to its higher solid-state Li diffusivity, smaller particle size, sloping OCV profile, and lower electrode tortuosity, the hard carbon anode exhibits a more uniform current density distribution than the graphite anode. In the future, a detailed investigation will be conducted to individually examine the effects of these factors on the current distribution.

By blending graphite and hard carbon, the resulting Gr-50 hybrid anode exhibits a significant improvement in the homogeneity of the current density distribution (Figure 6b), as compared to the graphite anode. To demonstrate that the hard carbon component within Gr-50 enables this improvement, we examined the evolution of the local current density for the graphite and

hard carbon constituents of Gr-50 anode, as shown in Figure 6d and 6e. Individually, the current density distribution follows the qualitative trend of the non-blend anodes. For the graphite component, most of the reaction takes place in the region near the anode/separator interface, while for the hard carbon component, the reaction is distributed more uniformly. Nonetheless, there exists a complex interplay between the two constituents, which is evident in the evolution of the integrated current for each individual component (Figure S19). The graphite component does not significantly contribute to the reaction until ~80 seconds, as the bulk of the component is electrochemically inactive in the voltage range during that time period, except for the region near the anode/separator interface. On the other hand, the hard carbon component contributes a large fraction of the current throughout the charging. Even towards the end of the simulation (when the anode voltage reaches 0 V), the hard carbon supplies 54% of the total current, which in turn reduces the load on the graphite component. In fact, the maximum surface current density of the graphite particles in the Gr-50 anode is 1.3 mA/cm^2, as compared to 1.6 mA/cm^2 for the pure graphite anode. Furthermore, these values occur at strikingly different times, 224 seconds for the Gr-50 anode vs. 61 seconds for the graphite anode.

Overall, the enhanced fast-charge capability of hybrid anodes is attributed to the improved homogeneity of reaction current, which originates from the interplay between the graphite and hard carbon constituents. While the more positive potential of hard carbon (compared to graphite) is often regarded as a disadvantage that limits energy density, in the case of the hybrid anode design, this drawback can be turned into an advantage. During the early stage of fast charging, the preferential lithiation of hard carbon particles and their enhanced rate capability reduces the current load on graphite particles, and lowers their propensity for Li plating. As charging continues, graphite particles progressively lithiate and contribute to the total accessible capacity of the hybrid anodes.

In order to quantify the degree of reaction homogeneity, we define H_{90} as the fraction of the anode volume that contributes to 90% of the current (integrated from the anode/separator interface). If the current density is perfectly uniform throughout the anode thickness, H_{90} would be 0.9. For the graphite anode, H_{90} rapidly decreases from 0.86 to 0.61 during charging (Figure S20). On the other hand, for the hard carbon and Gr-50 anode, the H_{90} remains above 0.77 and 0.71, respectively (Figure S20). The increase in the H_{90} value of the Gr-50 anode over the pure graphite anode clearly demonstrates the synergistic impact of hybrid anode design, which enables fast charging in energy-dense anodes.

2.7. Energy Density Retention during Long-term Fast-charge Cycling

To evaluate long-term cycling performance and energy density retention, pouch cells were cycled at 4C and 6C charge rates for 500 cycles. To measure the specific energy (gravimetric energy density) of the pouch cells, periodic capacity checks were performed after every 50 fast-charge cycles. In each capacity check, pouch cells were charged/discharged at a C/3 rate between 2.7-4.2 V to measure the capacity, voltage, and energy. **Figure 7** shows the stack specific energy of the pouch cells before fast-charge cycling and after 50, 200, and 500 cycles of fast charging. The stack specific energy accounts for the mass of all cell components except the pouch bag, excess electrolyte, and tab extensions (Figure S13). Stack specific energy is used because it is reduces dependency on the total cell capacity.[60] As shown in Figure 7, the graphite, Gr-75, Gr-50, Gr-25, and hard carbon cells have an initial stack specific energy of 202, 196, 180, 161, and 142 Wh/kg, respectively.

Due to Li plating during fast charging, the specific energy of the graphite and Gr-75 cells plunge to 135 Wh/kg and 160 Wh/kg after only 50 cycles of 4C charging (Figure 7a). The

specific energy loss is even more dramatic during 6C charging, as the graphite and Gr-75 cells maintain only 100 Wh/kg and 134 Wh/kg after 50 cycles (Figure 7b). In contrast, the Gr-50, Gr-25, and hard carbon cells demonstrate stable cycling at both 4C and 6C charge rates with minimal loss in specific energy. Among all 5 types of pouch cells, the Gr-50 cells maintain the highest specific energy throughout the 500 cycles of fast-charge cycling at both 4C and 6C charge rates.

It is therefore concluded that although high-specific-energy (> 200 Wh/kg) Li-ion batteries can be achieved using graphite anodes, significant Li loss upon fast charging quickly reduces the available energy density. Compared to the initial specific energy, the energy retention of the graphite cells is only 61% and 48% after 500 cycles of 4C and 6C charging, as shown in **Table 1-2** (also see Figure S14). In contrast, by rationally tuning the blend ratio of graphite/hard carbon in the hybrid anodes, the Gr-50 cells can achieve an initial specific energy of 180 Wh/kg, while maintaining an energy retention as high as 87% and 82% after 500 cycles of 4C and 6C fast-charge cycling (Table 1-2 and Figure S14). Therefore, while the Gr-50 hybrid cells show 10% lower initial specific energy compared to graphite cells, the remaining specific energy after 500 cycles of fast charging is 27% larger in the hybrid cell at 4C and 53% larger at 6C (Table 1-2). This demonstrates that the hybrid anode strategy is effective in overcoming energy and power density tradeoffs in Li-ion batteries.

3. Conclusion

In summary, we have demonstrated hybrid anodes fabricated by mixing graphite and hard carbon to achieve fast-charging Li-ion batteries with high energy densities (>180 Wh/kg), using industrially relevant multi-layer pouch cells (> 1 Ah) and electrode capacity loadings (3 mAh/cm^2). By tuning the blend ratio of graphite/hard carbon, it is shown that hybrid anodes with improved current homogeneity and reduced Li plating during fast charging can be

achieved, while maintaining sufficiently high energy densities. For a 3 mAh/cm^2 anode loading under 4C-6C charging conditions, our analysis indicates that the 50/50 graphite/hard carbon blend ratio provides the maximum performance within the set of ratios tested. With the Gr-50 anode, we have demonstrated pouch cells with 87% and 82% specific energy retention after 500 cycles of 4C and 6C fast-charge cycling, compared to 61% and 48% for cells using graphite anodes under the same conditions. In addition, while the Gr-50 cells show 10% lower initial specific energy compared to the graphite cells, the remaining specific energy after 500 cycles of fast charging is 27% larger at 4C and 53% larger at 6C. Therefore, the hybrid anode design significantly reduces tradeoffs between energy and power density.

Systematic electrochemical analysis was performed to demonstrate the efficacy of the hybrid anode design. Continuum-scale electrochemical simulations identified the origin of the enhanced fast-charge performance to be the improved homogeneity in reaction current distribution throughout the hybrid anode volume. Moreover, synchrotron tomography showed that while the graphite and hard carbon are uniformly blended throughout the bulk of the electrode, subtle differences in the local microstructures can be observed, which may further impact the local current density variation within the electrodes. In the future, detailed modeling studies will be performed to further decouple the contributing variables to the improved power performance of the hybrid cells.

Importantly, standard mixing, roll-to-roll slurry casting, and calendaring was performed here to fabricate the hybrid anodes, demonstrating direct compatibility with existing Li-ion manufacturing. This is a significant advantage of the hybrid anode approach, as it does not require developing alternative processing methods or device architectures, which could result additional manufacturing costs and/or reduce throughput. By overcoming energy and power

density tradeoffs in Li-ion batteries, the hybrid anode design provides a pathway toward efficient fast-charging of high-energy-density EV-scale batteries.

Supporting Information
Supporting Information is available from the Wiley Online Library or from the author.

Acknowledgements
The authors acknowledge support from the Office of Energy Efficiency and Renewable Energy (EERE) of the U.S. Department of Energy, under Award Number DE-EE0008362. This work was performed in part at the University of Michigan Battery Lab, and the authors would like to thank Greg Less, William Hicks, and Arthur Sinclair for their assistance on the pouch cell fabrication. The authors acknowledge and thank Pred Materials International for supplying the hard carbon material for this research. We thank Dr. Eric Kazyak for help in preparing the 3-D electrode schematics and Yuxin Chen for performing optical microscopy. We acknowledge the Paul Scherrer Institut, Villigen, Switzerland for provision of synchrotron radiation beamtime at the TOMCAT beamline X02DA of the SLS and would like to thank Dr. Federica Marone for assistance. The authors acknowledge the financial support from the University of Michigan College of Engineering, technical support from the Michigan Center for Materials Characterization, and computational resources at the University of Michigan College of Engineering CAEN.

Received: ((will be filled in by the editorial staff))
Revised: ((will be filled in by the editorial staff))
Published online: ((will be filled in by the editorial staff))

References

[1] S. Ahmed, I. Bloom, A. N. Jansen, T. Tanim, E. J. Dufek, A. Pesaran, A. Burnham, R. B. Carlson, F. Dias, K. Hardy, M. Keyser, C. Kreuzer, A. Markel, A. Meintz, C. Michelbacher, M. Mohanpurkar, P. A. Nelson, D. C. Robertson, D. Scoffield, M. Shirk, T. Stephens, R. Vijayagopal, J. Zhang, *J. Power Sources* **2017**, *367*, 250.
[2] M. Keyser, A. Pesaran, Q. Li, S. Santhanagopalan, K. Smith, E. Wood, S. Ahmed, I. Bloom, E. Dufek, M. Shirk, A. Meintz, C. Kreuzer, C. Michelbacher, A. Burnham, T. Stephens, J. Francfort, B. Carlson, J. Zhang, R. Vijayagopal, K. Hardy, F. Dias, M. Mohanpurkar, D. Scoffield, A. N. Jansen, T. Tanim, A. Markel, *J. Power Sources* **2017**, *367*, 228.
[3] T. Waldmann, B. I. Hogg, M. Wohlfahrt-Mehrens, *J. Power Sources* **2018**, *384*, 107.
[4] M. Winter, B. Barnett, K. Xu, *Chem. Rev.* **2018**, *118*, 11433.
[5] X. Zeng, M. Li, D. Abd El-Hady, W. Alshitari, A. S. Al-Bogami, J. Lu, K. Amine, *Adv. Energy Mater.* **2019**, *9*, 1900161.
[6] C. Mao, M. Wood, L. David, S. J. An, Y. Sheng, Z. Du, H. M. Meyer, R. E. Ruther, D. L. Wood, *J. Electrochem. Soc.* **2018**, *165*, A1837.
[7] G. E. Blomgren, *J. Electrochem. Soc.* **2017**, *164*, A5019.
[8] W. Mai, A. M. Colclasure, K. Smith, *J. Electrochem. Soc.* **2020**, *167*, 080517.
[9] A. M. Colclasure, A. R. Dunlop, S. E. Trask, B. J. Polzin, A. N. Jansen, K. Smith, *J. Electrochem. Soc.* **2019**, *166*, A1412.

[10] A. M. Colclasure, T. R. Tanim, A. N. Jansen, S. E. Trask, A. R. Dunlop, B. J. Polzin, I. Bloom, D. Robertson, L. R. Flores, M. Evans, E. J. Dufek, K. Smith, *Electrochim. Acta* **2020**, *337*, 135854.
[11] V. P. Nemani, S. J. Harris, K. C. Smith, *J. Electrochem. Soc.* **2015**, *162*, A1415.
[12] S. J. Harris, P. Lu, *J. Phys. Chem. C* **2013**, *117*, 6481.
[13] K. Chen, M. J. Namkoong, V. Goel, C. Yang, S. Kazemiabnavi, S. M. Mortuza, E. Kazyak, J. Mazumder, K. Thornton, J. Sakamoto, N. P. Dasgupta, *J. Power Sources* **2020**, *471*, 228475.
[14] Z. M. Konz, E. J. McShane, B. D. McCloskey, *ACS Energy Lett.* **2020**, *5*, 1750.
[15] E. J. McShane, E. J. McShane, A. M. Colclasure, D. E. Brown, D. E. Brown, Z. M. Konz, Z. M. Konz, K. Smith, B. D. McCloskey, B. D. McCloskey, *ACS Energy Lett.* **2020**, *5*, 2045.
[16] X. G. Yang, T. Liu, Y. Gao, S. Ge, Y. Leng, D. Wang, C.-Y. Y. Wang, *Joule* **2019**, *3*, 3002.
[17] K. G. Gallagher, S. E. Trask, C. Bauer, T. Woehrle, S. F. Lux, M. Tschech, P. Lamp, B. J. Polzin, S. Ha, B. Long, Q. Wu, W. Lu, D. W. Dees, A. N. Jansen, *J. Electrochem. Soc.* **2016**, *163*, A138.
[18] L. Li, R. M. Erb, J. Wang, J. Wang, Y. Chiang, *Adv. Energy Mater.* **2019**, *9*, 1802472.
[19] Y. Kim, A. Drews, R. Chandrasekaran, T. Miller, J. Sakamoto, *Ionics (Kiel).* **2018**, *24*, 2935.
[20] E. R. Logan, J. R. Dahn, *Trends Chem.* **2020**, *2*, 354.
[21] D. S. Hall, A. Eldesoky, E. R. Logan, E. M. Tonita, X. Ma, J. R. Dahn, *J. Electrochem. Soc.* **2018**, *165*, A2365.
[22] K. M. Diederichsen, E. J. McShane, B. D. McCloskey, *ACS Energy Lett.* **2017**, *2*, 2563.
[23] K. R. Tallman, B. Zhang, L. Wang, S. Yan, K. Thompson, X. Tong, J. Thieme, A. Kiss, A. C. Marschilok, K. J. Takeuchi, D. C. Bock, E. S. Takeuchi, *ACS Appl. Mater. Interfaces* **2019**, *11*, 46864.
[24] K. Kubota, S. Shimadzu, N. Yabuuchi, S. Tominaka, S. Shiraishi, M. Abreu-Sepulveda, A. Manivannan, K. Gotoh, M. Fukunishi, M. Dahbi, S. Komaba, *Chem. Mater.* **2020**, *32*, 2961.
[25] E. Buiel, J. R. Dahn, *Electrochim. Acta* **1999**, *45*, 121.
[26] D. A. Stevens, J. R. Dahn, *J. Electrochem. Soc.* **2001**, *148*, A803.
[27] E. Irisarri, A. Ponrouch, M. R. Palacin, *J. Electrochem. Soc.* **2015**, *162*, A2476.
[28] A. Shellikeri, V. Watson, D. Adams, E. E. Kalu, J. A. Read, T. R. Jow, J. S. P. S. Zheng, J. S. P. S. Zheng, *J. Electrochem. Soc.* **2017**, *164*, A3914.
[29] K. Guerin, A. Fevrier-Bouvier, S. Flandrois, B. Simon, P. Biensan, *Electrochim. Acta* **2000**, *45*, 1607.
[30] C. Matei Ghimbeu, J. Górka, V. Simone, L. Simonin, S. Martinet, C. Vix-Guterl, *Nano Energy* **2018**, *44*, 327.
[31] T. Horiba, T. Maeshima, T. Matsumura, M. Koseki, J. Arai, Y. Muranaka, *J. Power Sources* **2005**, *146*, 107.
[32] Y. Nishi, *Electrochem. Soc. Interface* **2016**, *25*, 71.
[33] C. Ge, J. Wang, Z. Fan, J. Zhang, Y. Qiao, **2018**, 34682.
[34] Y. G. Lim, J. W. Park, M. S. Park, D. Byun, J. S. Yu, Y. N. Jo, Y. J. Kim, *Bull. Korean Chem. Soc.* **2015**, *36*, 150.
[35] K. J. Kim, T. S. Lee, H. G. Kim, S. H. Lim, S. M. Lee, *Electrochim. Acta* **2014**, *135*, 27.
[36] K. Yanagida, A. Yanai, Y. Kida, A. Funahashi, T. Nohma, I. Yonezu, *J. Electrochem. Soc.* **2002**, *149*, A804.
[37] A. Kinoshita, K. Yanagida, A. Yanai, Y. Kida, A. Funahashi, T. Nohma, I. Yonezu, *J.*

Power Sources **2001**, *102*, 283.
[38] R. Schmuch, R. Wagner, G. Hörpel, T. Placke, M. Winter, *Nat. Energy* **2018**, *3*, 267.
[39] S. J. Harris, A. Timmons, D. R. Baker, C. Monroe, *Chem. Phys. Lett.* **2010**, *485*, 265.
[40] Y. Qi, S. J. Harris, *J. Electrochem. Soc.* **2010**, *157*, A741.
[41] V. Wood, *Nat. Rev. Mater.* **2018**, *3*, 293.
[42] S. Müller, J. Eller, M. Ebner, C. Burns, J. Dahn, V. Wood, *J. Electrochem. Soc.* **2018**, *165*, A339.
[43] P. Pietsch, M. Ebner, F. Marone, M. Stampanoni, V. Wood, *Sustain. Energy Fuels* **2018**, *2*, 598.
[44] D. Kehrwald, P. R. Shearing, N. P. Brandon, P. K. Sinha, S. J. Harris, *J. Electrochem. Soc.* **2011**, *158*, A1393.
[45] G. Harauz, M. Van Heel, *Opt.* **1986**, *73*, 146.
[46] K. G. Gallagher, D. W. Dees, A. N. Jansen, D. P. Abraham, S.-H. Kang, *J. Electrochem. Soc.* **2012**, *159*, A2029.
[47] J. R. Dahn, *Phys. Rev. B* **1991**, *44*, 9170.
[48] J. Kasnatscheew, M. Evertz, B. Streipert, R. Wagner, R. Klöpsch, B. Vortmann, H. Hahn, S. Nowak, M. Amereller, A. C. Gentschev, P. Lamp, M. Winter, *Phys. Chem. Chem. Phys.* **2016**, *18*, 3956.
[49] H. Zhou, F. Xin, B. Pei, M. S. Whittingham, *ACS Energy Lett.* **2019**, *4*, 1902.
[50] Battery Test Manual For Electric Vehicles, **2015**.
[51] K.-H. Chen, K. N. Wood, E. Kazyak, W. S. LePage, A. L. Davis, A. J. Sanchez, N. P. Dasgupta, *J. Mater. Chem. A* **2017**, *5*, 11671.
[52] J. S. Newman, C. W. Tobias, *J. Electrochem. Soc.* **1962**, *109*, 1183.
[53] J. Newman, W. Tiedemann, *AIChe J.* **1975**, *21*, 25.
[54] M.-T. F. Rodrigues, K. Kalaga, S. E. Trask, D. W. Dees, I. A. Shkrob, D. P. Abraham, *J. Electrochem. Soc.* **2019**, *166*, A996.
[55] Q. Liu, C. Du, B. Shen, P. Zuo, X. Cheng, Y. Ma, G. Yin, Y. Gao, *RSC Adv.* **2016**, *6*, 88683.
[56] D. Tewari, Z. Liu, P. B. Balbuena, P. P. Mukherjee, *J. Phys. Chem. C* **2018**, *122*, 21097.
[57] T. F. Fuller, *J. Electrochem. Soc.* **1994**, *141*, 1.
[58] M. Doyle, T. F. Fuller, J. Newman, *Electrochim. Acta* **1994**, *39*, 2073.
[59] M. Doyle, J. Newman, *J. Power Sources* **1995**, *54*, 46.
[60] J. E. Harlow, X. Ma, J. Li, E. Logan, Y. Liu, N. Zhang, L. Ma, S. L. Glazier, M. M. E. Cormier, M. Genovese, S. Buteau, A. Cameron, J. E. Stark, J. R. Dahn, *J. Electrochem. Soc.* **2019**, *166*, A3031.

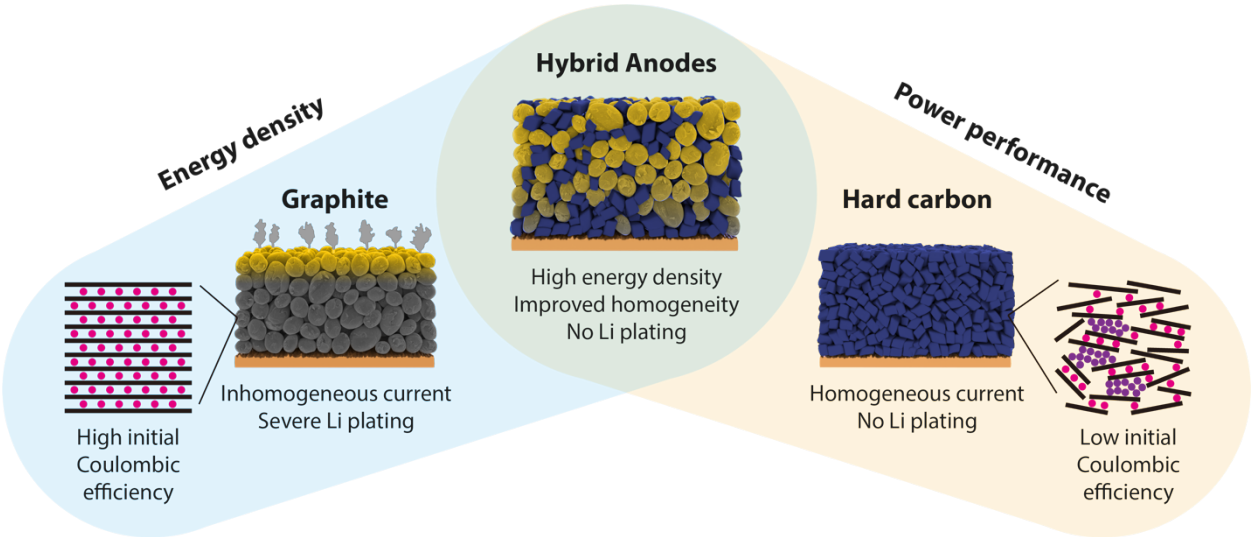

Scheme 1. Schematic illustration of the energy/power density tradeoff between graphite and hard carbon. In this study, graphite/hard carbon hybrid anodes are shown to improve current homogeneity and reduce Li plating during fast charging, while maintaining high energy densities. Lithiated graphite and hard carbon particles are indicated by gold and blue colors, respectively.

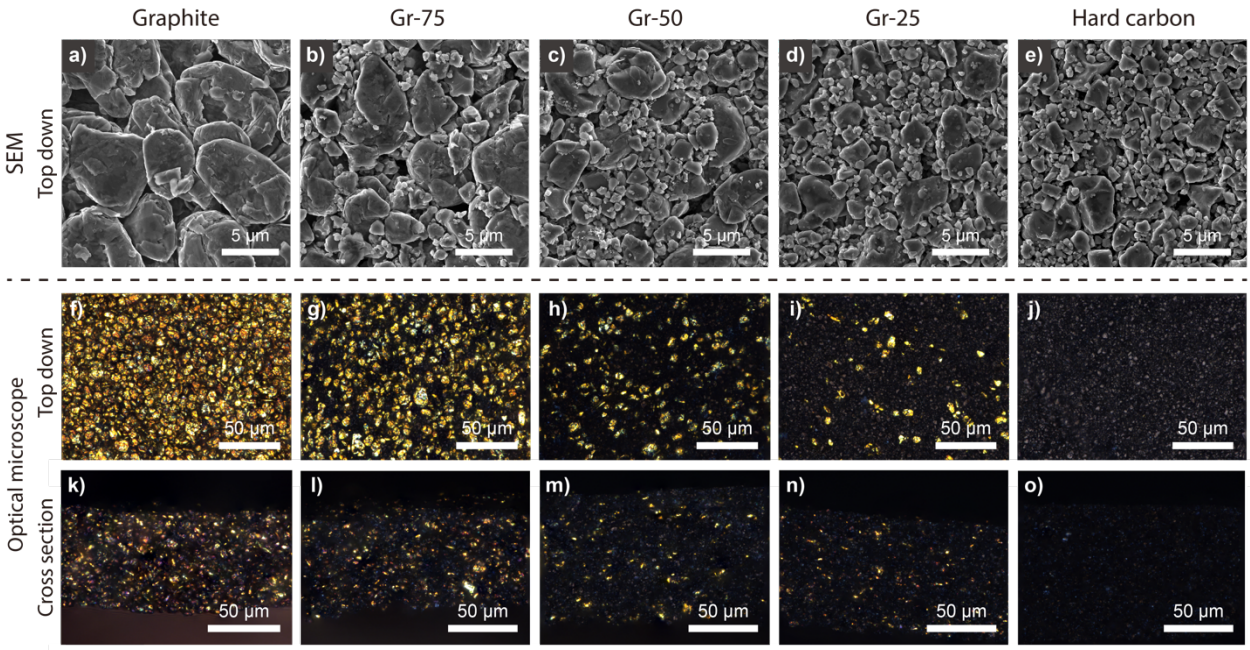

Figure 1. Top-down SEM images of the (a) graphite, (b) Gr-75, (c) Gr-50, (d) Gr-25, and (e) hard carbon anodes. Top-down and cross-sectional optical microscope images of the lithiated (f,k) graphite, (g,l) Gr-75, (h,m) Gr-50, (i,n) Gr-25, and (j,o) hard carbon electrodes, respectively.

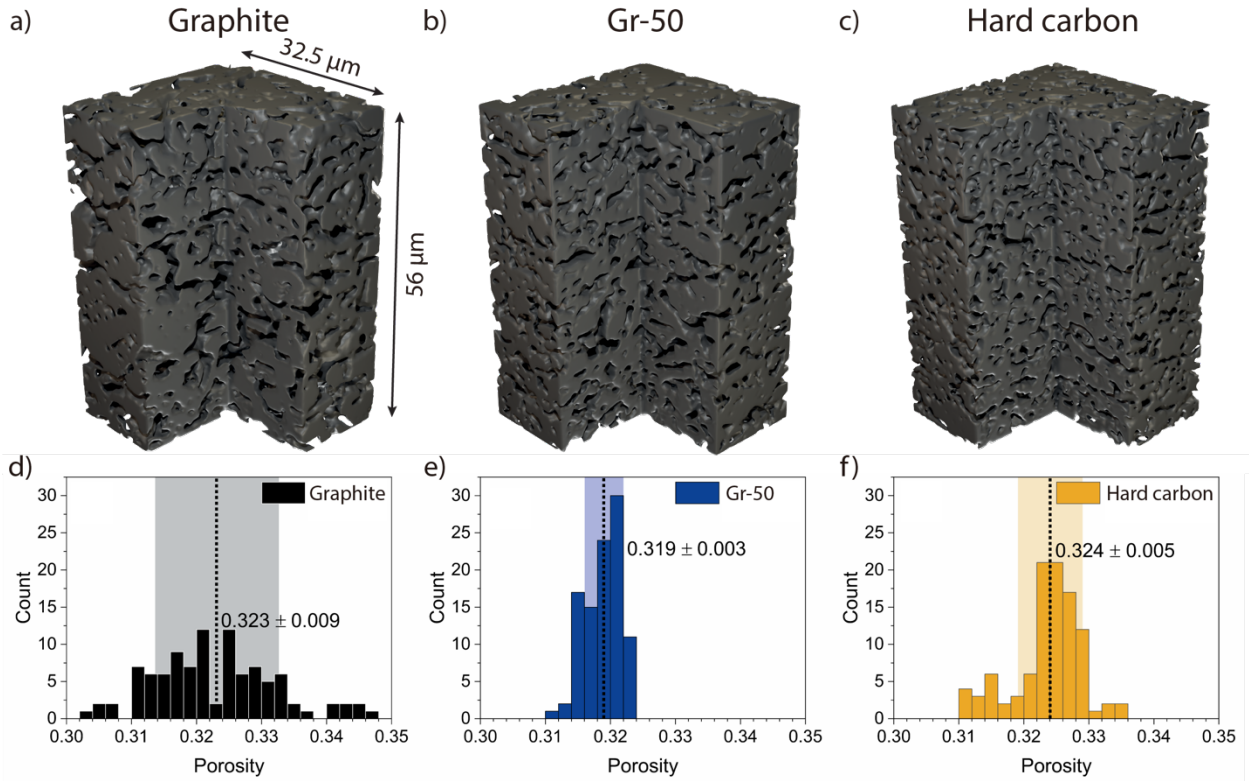

Figure 2. 3-D representations of the segmented tomography data with 32.5 µm x 32.5 µm x 56 µm edge length of the (a) graphite, (b) Gr-50, and (c) hard carbon electrodes. The solid particle phase is represented in grey. Porosity histograms of 100 cubic representative sub-volumes with an edge length of 56 µm of the (d) graphite, (e) Gr-50, and (f) hard carbon electrodes. The average porosity of all electrode segmentations is ~32%.

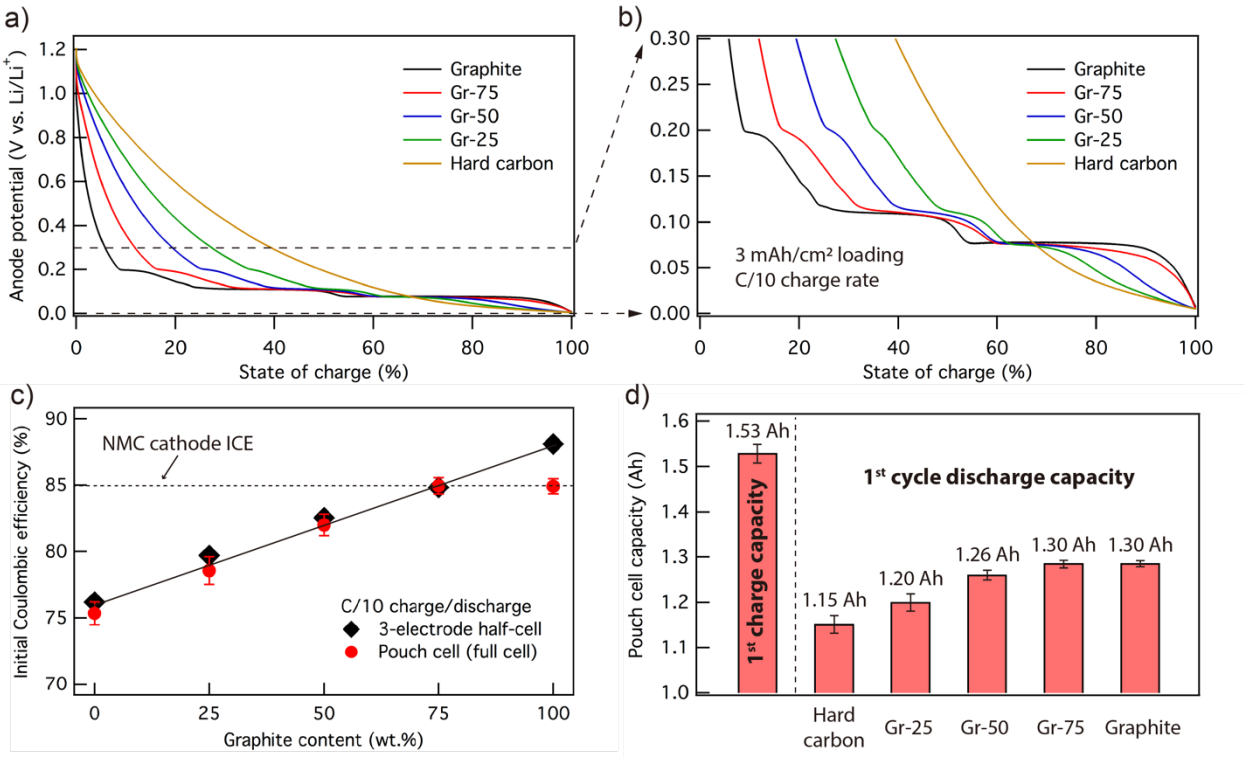

Figure 3. (a-b) Three-electrode measurements showing the anode potential (V vs. Li/Li^+) as a function of state-of-charge for graphite, Gr-75, Gr-50, Gr-25, and hard carbon. (c) Initial Coulombic efficiency (ICE) vs. graphite content plot of the hybrid anodes in 3-electrode cell (black) and pouch cell (red) configurations. The ICE of NMC-532 cathode is also labeled in the plot. The charge/discharge rate was fixed at C/10. (d) Cell capacity plot showing the first-cycle charge and discharge capacity of the pouch cells.

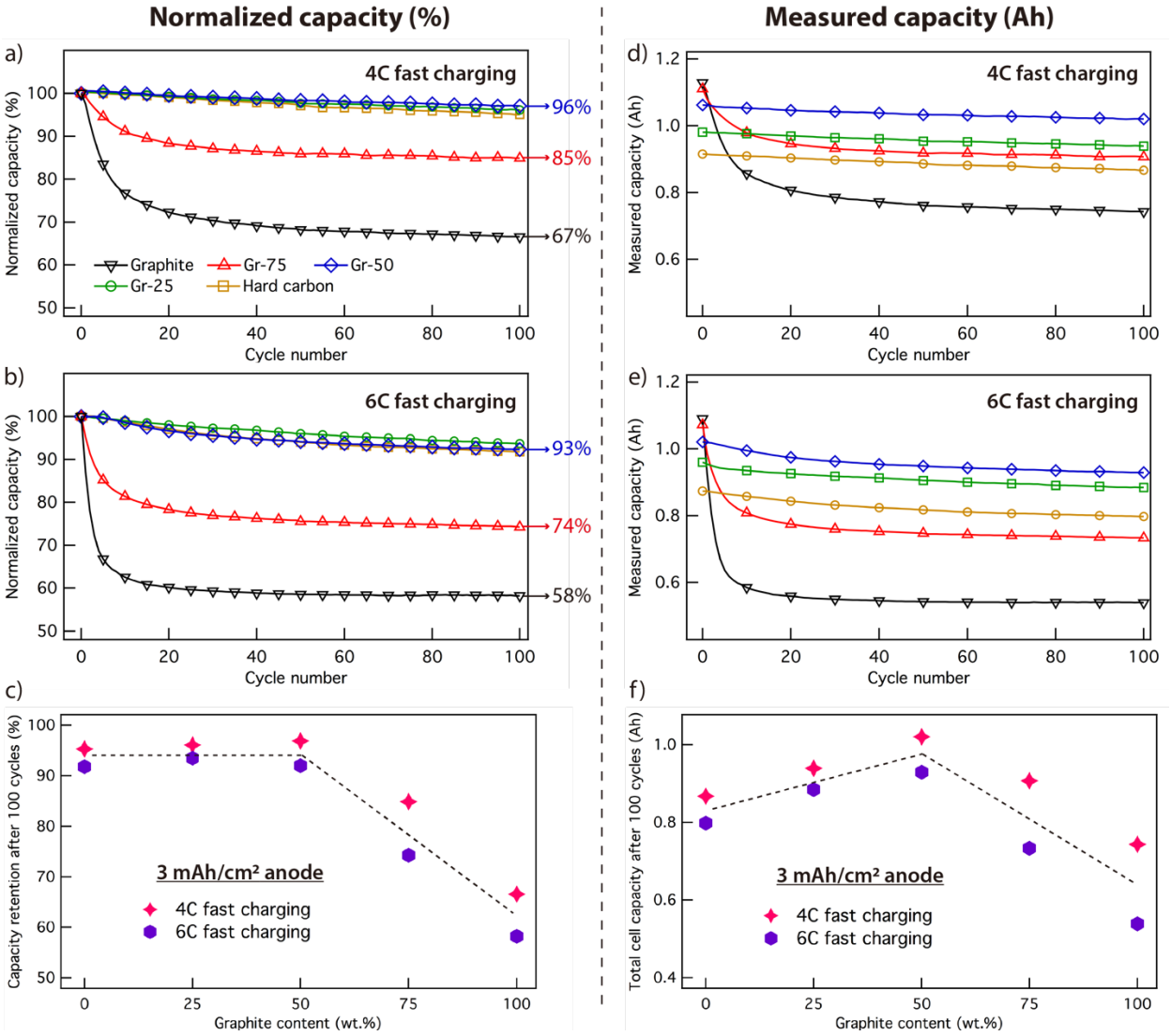

Figure 4. Normalized capacity vs. cycle number plots during (a) 4C and (b) 6C fast-charge cycling. The capacity retention after 100 fast-charge cycles is indicated as a percentage to the right of the plots. (c) Summary of the capacity retention (%) after 100 cycles of 4C and 6C fast charging. Measured capacity vs. cycle number plots during (d) 4C and (e) 6C fast-charge cycling. (f) Summary of total cell capacity (Ah) after 100 cycles of 4C and 6C fast charging. The capacity shown here is the 1C discharge capacity after each charge half cycle.

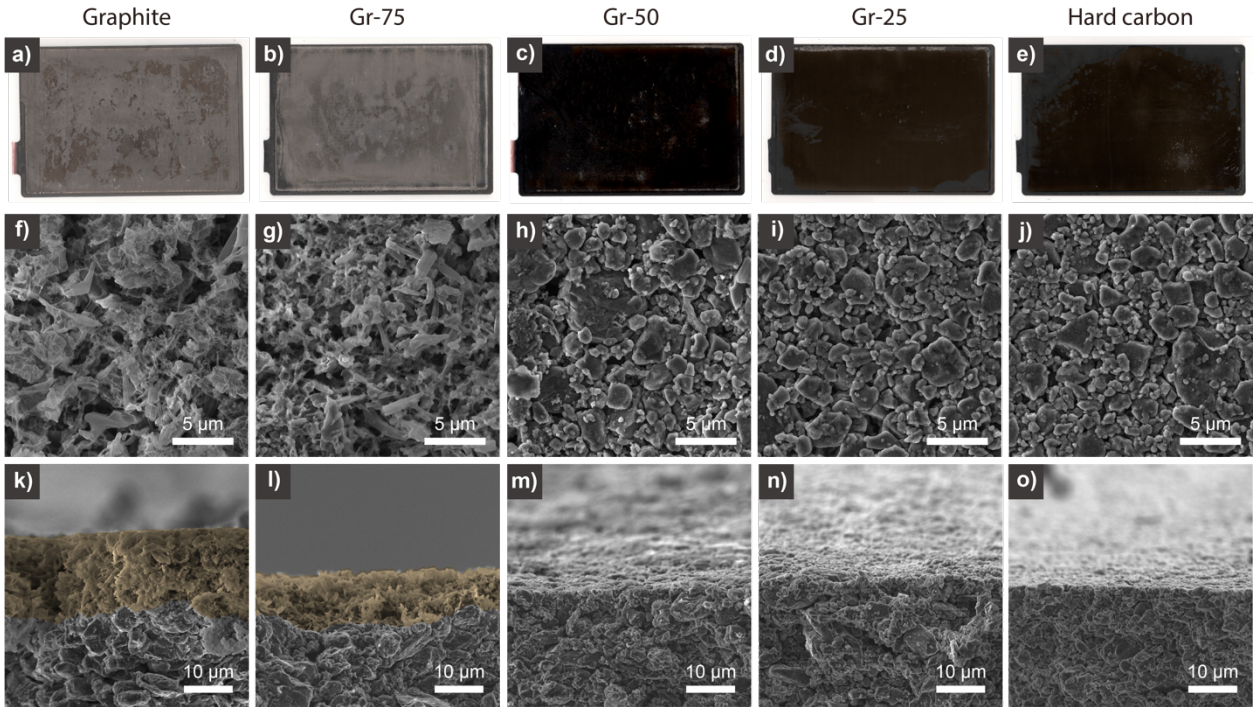

Figure 5. (a-e) Photographs of the cycled anodes from pouch cell teardown after 100 cycles of 4C fast charging. SEM analysis further show the (f-j) top-down and (k-o) cross-sectional images. Li plating on the graphite and Gr-75 anodes is false-colored in yellow in Figure k and l.

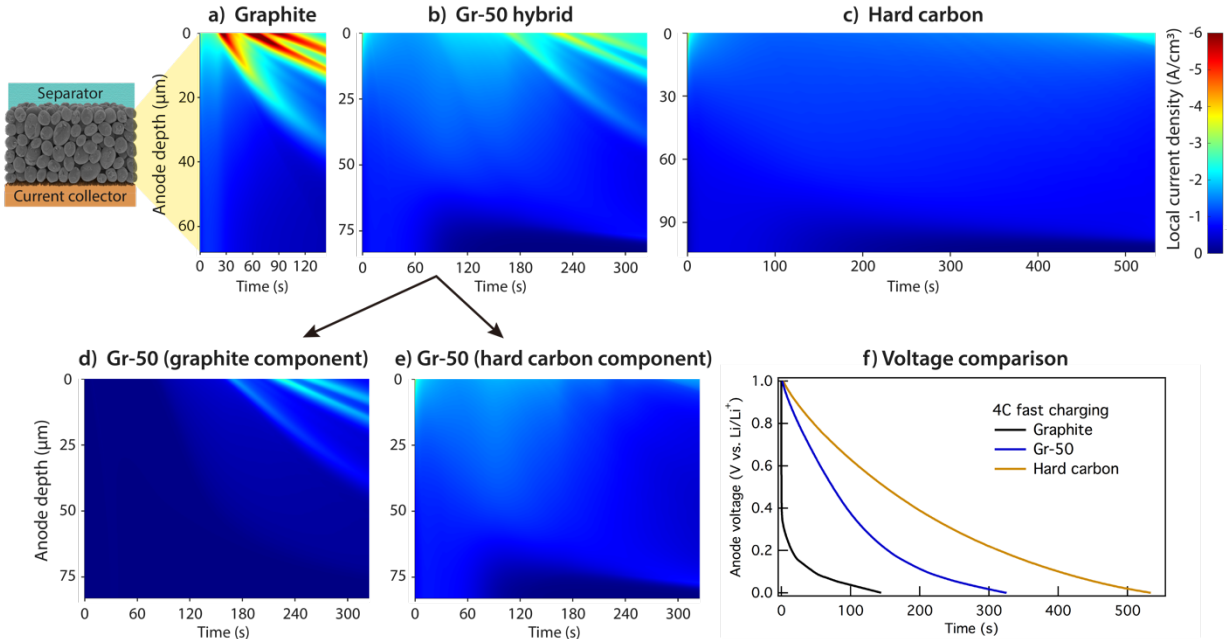

Figure 6. Evolution of the local reaction current density as a function of the position through the thickness of the (a) graphite, (b) Gr-50, and (c) hard carbon anodes during 4C charging. The schematic on the left of panel (a) shows the orientation of the anodes in the evolution plots. The top edge and the bottom edge of each evolution plot correspond to the anode/separator and anode/current collector interfaces, respectively. (d-e) Evolution of the local current density contribution by the graphite and hard carbon components in the Gr-50 anode. The maximum magnitude of the reaction current density on the color bar is limited to 6 A/cm^3 to enable a better visual comparison among the three anodes (the maximum magnitude of the reaction current density observed in the graphite anode is 8 A/cm^3). Therefore, the dark red regions in the graphite plot have values between -6 A/cm^3 and -8 A/cm^3. (f) Comparison of the simulated voltage vs. time plots during 4C charging for the three anodes.

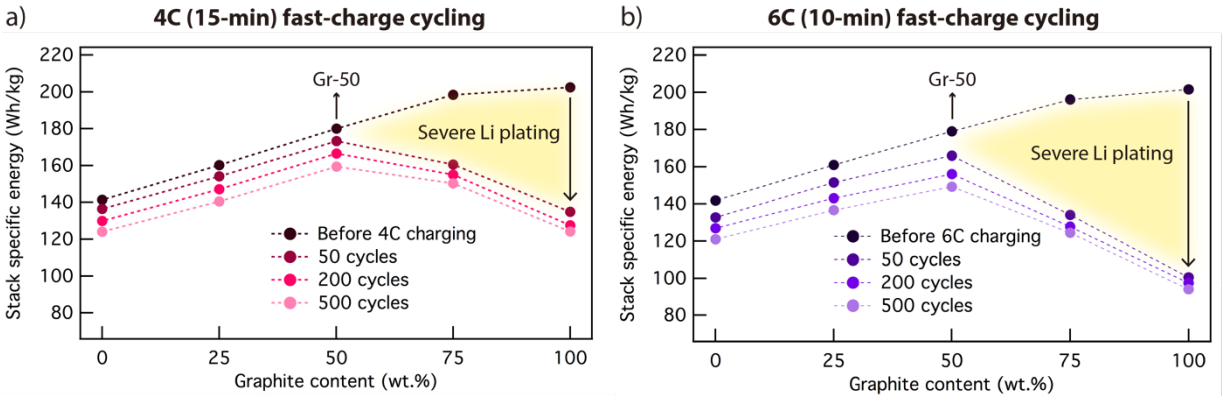

Figure 7. Stack specific energy vs. graphite content during (a) 4C (15-min) and (b) 6C (10-min) long-term fast-charge cycling. Specific energy before cycling and after 50, 200, and 500 cycles of fast charging is shown for the pouch cells with varying graphite content. Cell specific energy was measured at C/3 charge/discharge rates periodically throughout the fast-charging cycling.

4C fast charging	Initial (Wh/kg)	After 500 cycles (Wh/kg)	Energy retention (%)
Graphite	202	124	61%
Gr-50	180	157	87%
Improvement (%)	-10%	+27%	

Table 1. Stack specific energy retention and improvement between the graphite and Gr-50 cells during 4C fast-charge cycling.

6C fast charging	Initial (Wh/kg)	After 500 cycles (Wh/kg)	Energy retention (%)
Graphite	202	97	48%
Gr-50	180	148	82%
Improvement (%)	-10%	+53%	

Table 2. Stack specific energy retention and improvement between the graphite and Gr-50 cells during 6C fast-charge cycling.

Enabling 6C Fast Charging of Li-ion Batteries with Graphite/Hard Carbon Hybrid Anodes

Kuan-Hung Chen, Vishwas Goel, Min Ji Namkoong, Markus Wied, Simon Müller, Vanessa Wood, Jeff Sakamoto, Katsuyo Thornton, Neil P. Dasgupta*

Hybrid anodes fabricated by mixing graphite and hard carbon are demonstrated to achieve fast-charging Li-ion batteries with high energy densities, using industrially relevant multi-layer pouch cells (> 1 Ah). By tuning the blend ratio of graphite/hard carbon, pouch cells with 180 Wh/kg energy density and 87%/82% energy retention after 500 cycles of 4C/6C fast-charge cycling are achieved.